



## Fabrication of bimetallic Hofmann-type metal-organic Frameworks@Cellulose aerogels for efficient iodine capture

Yuhang Wu, Yuanbo Xie, Fangyuan Zhong, Junkuo Gao<sup>\*</sup>, Juming Yao<sup>\*\*</sup>

*Institute of Fiber Based New Energy Materials, The Key Laboratory of Advanced Textile Materials and Manufacturing Technology of Ministry of Education, School of Materials Science and Engineering, Zhejiang Sci-Tech University, Hangzhou, 310018, China*

### ARTICLE INFO

#### Keywords:

Metal-organic frameworks  
Hybrid aerogels  
Iodine adsorption  
Doping method  
Hofmann-type

### ABSTRACT

It is of great significance to capture radioiodine from nuclear-related activities. Herein, We fabricated two kinds of hybrid aerogels composed with bimetal Hofmann-type metal-organic frameworks (Co-Fe)<sup>II</sup>(pz)[Ni<sup>II</sup>(CN)<sub>4</sub>] and cellulose aerogels by in-situ growth and doping method (named CoFe@CA-IS and CoFe@CA-D, respectively). The hybrid aerogels possessed excellent iodine adsorption performance. The addition of (Co-Fe)<sup>II</sup>(pz)[Ni<sup>II</sup>(CN)<sub>4</sub>] increased the porosity of the hybrid aerogels. The porosities of CoFe@CA-IS and CoFe@CA-D were reached 86.7% and 87.8%, respectively, which are higher than pure cellulose aerogels. Furthermore, the doping method provide a significant improve of adsorption performance. The equilibrium adsorption capacity of CoFe@CA-D reached 457.99 mg g<sup>-1</sup> and the equilibrium adsorption capacity of CoFe@CA-IS was 194.34 mg g<sup>-1</sup>. In addition, the hybrid aerogels showed excellent recycle ability, the equilibrium adsorption capacity of CoFe@CA-IS and CoFe@CA-D remained 81% and 91% after 5 cycles. The results suggested that this metal-organic framework@cellulose hybrid aerogel showed great potential in iodine treatment and could be applied in a wide field.

### 1. Introduction

Since the beginning of the new century, with the depletion of fossil fuels, climate and energy issues have received much attention, and new energy sources have been favored. Among them, nuclear energy will be widely used due to its safety, clean and high energy density [1–4]. However, nuclear waste produces some radioactive elements such as <sup>129</sup>I and <sup>131</sup>I, <sup>129</sup>I has a half-life of 1.57 × 10<sup>7</sup> years, which can cause persistent damage to the environment [5–8]. Radioactive iodine can produce  $\gamma$ -rays during decay, causing sustained damage to the human healthy and the environment [9–11]. It is very crucial to capture radioactive iodine.

Metal-organic frameworks (MOFs) are a kind of porous material prepared from self-assembled metal ions or clusters and organic ligands with 1D, 2D, or 3D topological structure [12–14]. MOFs have a series of advantages such as large specific surface area, adjustable structure, and abundant active sites, which are attracted widespread attention in adsorption, separation, catalysis, and fluorescence sensing [15–18]. As potential adsorbents, MOF have received extensive attention in the field of iodine adsorption [19–23]. Among various MOFs, the Hofmann-type

MOFs composed of transition metals and transition metal cyanates (the structural formula is M<sup>II</sup>(pz)[N<sup>II</sup>(CN)<sub>4</sub>] (pz = pyrazine, M = Ni<sup>2+</sup>, Co<sup>2+</sup>, Fe<sup>2+</sup>; N = Ni<sup>2+</sup>, Pd<sup>2+</sup>, Pt<sup>2+</sup>)), contain a large number of cyano groups and adsorption sites [24]. It has been proved that Ni<sup>II</sup>(pz)[Ni<sup>II</sup>(CN)<sub>4</sub>] shows a good adsorption effect on iodine, and the adsorption capacity reaches 1 mol of I<sub>2</sub> per mole of Hofmann-type structure MOFs [25]. Furthermore, the introduction of secondary metal nodes in MOFs can improve the adsorption capacity. On the one hand, the introduction of secondary metal nodes can produce defects to increase the adsorption sites. On the other hand, the synergy between different metals can also enhance the intrinsic properties of MOFs [26,27].

However, MOF crystals exist in the form of powder so that they are easy to agglomerate and difficult to recycle, which inhibit their development [28]. In order to overcome the above difficulties, it is an effective strategy to choose a suitable method to load MOFs. Generally, there should be a good interaction between the substrate and MOFs to ensure the MOFs are firmly bonded to the surface of the substrate, and the substrate should be easy to process and easy to separation [29,30]. Cellulose is an ideal substrate because it is a renewable resource with large reserves, easy processing and biodegradation [31–34]. Cellulose

<sup>\*</sup> Corresponding author.

<sup>\*\*</sup> Corresponding author.

E-mail addresses: [jkgao@zstu.edu.cn](mailto:jkgao@zstu.edu.cn) (J. Gao), [yaoj@zstu.edu.cn](mailto:yaoj@zstu.edu.cn) (J. Yao).

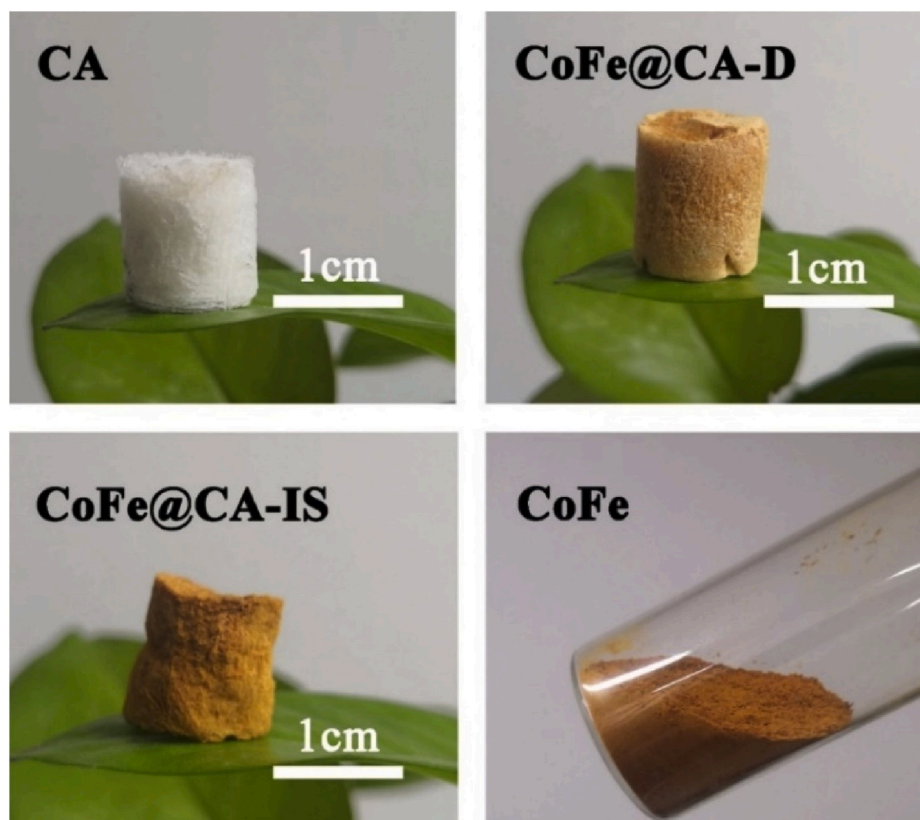


Fig. 1. Photographs of CA, CoFe@CA-D, CoFe@CA-IS and  $(\text{Co-Fe})^{\text{II}}(\text{pz})[\text{Ni}^{\text{II}}(\text{CN})_4]$ .

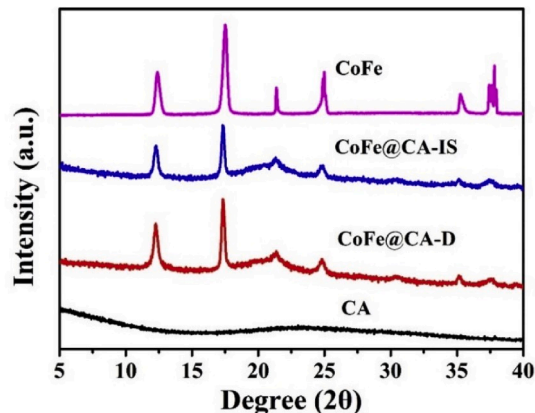


Fig. 2. The XRD patterns of the CA, CoFe@CA and CoFe.

aerogel (CA) is a flexible material with high porosity, high water stability, light weight and high strength [35,36]. Lei and Ren [37,38] have used the in-situ growth method to prepare high-load MOFs@CA composites, which have achieved good results in the adsorption of heavy metal ions and the degradation of organic pollutants.

In this paper, a second metal node was introduced in  $\text{M}^{\text{II}}(\text{pz})[\text{Ni}^{\text{II}}(\text{CN})_4]$  to prepare bimetallic Hofmann-type MOFs with the structural formula  $(\text{M-m})^{\text{II}}(\text{pz})[\text{Ni}^{\text{II}}(\text{CN})_4]$  ( $\text{M-m} = \text{Co}^{2+}\text{-Ni}^{2+}$ ,  $\text{Co}^{2+}\text{-Fe}^{2+}$ ,  $\text{Fe}^{2+}\text{-Ni}^{2+}$ ). The Hofmann@CA composites were prepared by in-situ growth and doping methods at room temperature, recorded as CoFe@CA-IS and CoFe@CA-D, respectively. The experimental results showed that  $(\text{Co-Fe})^{\text{II}}(\text{pz})[\text{Ni}^{\text{II}}(\text{CN})_4]$  (CoFe) had the best iodine adsorption performance. The doping method could increase the loading of  $(\text{Co-Fe})^{\text{II}}(\text{pz})[\text{Ni}^{\text{II}}(\text{CN})_4]$  (reach to 45.8%), which was larger than that of the CoFe@CA-IS (13.5%). The CoFe@CA-D had higher adsorption

performance for iodine, and the iodine adsorption amount reached  $457.99 \text{ mg g}^{-1}$ , which was larger than the adsorption amount of CoFe@CA-IS ( $194.34 \text{ mg g}^{-1}$ ).

## 2. Experimental

### 2.1. Materials and reagents

Cotton was purchased from Heze Sanmu Health Materials Co., Ltd. (Shandong, China).  $\text{Co}(\text{NO}_3)_2 \cdot 6\text{H}_2\text{O}$  was provided by Mclean Biochemical Technology Co., Ltd. (Shanghai, China).  $\text{Fe}(\text{ClO}_4)_2 \cdot x\text{H}_2\text{O}$  and pyrazine were provided by Sun Chemical Technology (Shanghai) Co., Ltd. (Shanghai, China).  $\text{K}_2[\text{Ni}^{\text{II}}(\text{CN})_4] \cdot x\text{H}_2\text{O}$  and  $\text{Ni}(\text{NO}_3)_2 \cdot 6\text{H}_2\text{O}$  were purchased by Sigma Aldrich (Shanghai) Trading Co., Ltd. Iodine and N,N'-methylenebisacrylamide (MBA) were purchased by Shanghai Aladdin Biotechnology Co., Ltd. (Shanghai, China). Hexane was supplied from Tianjin Yongda Chemical Reagent Co., Ltd. Methanol (MA) was supplied by Gaojing Fine Chemical Co., Ltd. (Hangzhou, China). All the chemical reagents were analytical grade and used without further purification.

### 2.2. Synthesis of cellulose aerogels

The preparation of cellulose aerogel was based on previous reports with slight modifications (see the SI).

### 2.3. Synthesis of Hofmann-type MOFs

The preparation of Hofmann-type MOFs was based on previous reports with slight modifications (see the SI and Fig. S1).

### 2.4. Synthesis of hybrid aerogels

In this paper,  $(\text{Co-Fe})^{\text{II}}(\text{pz})[\text{Ni}^{\text{II}}(\text{CN})_4]$ -loaded cellulose aerogel is

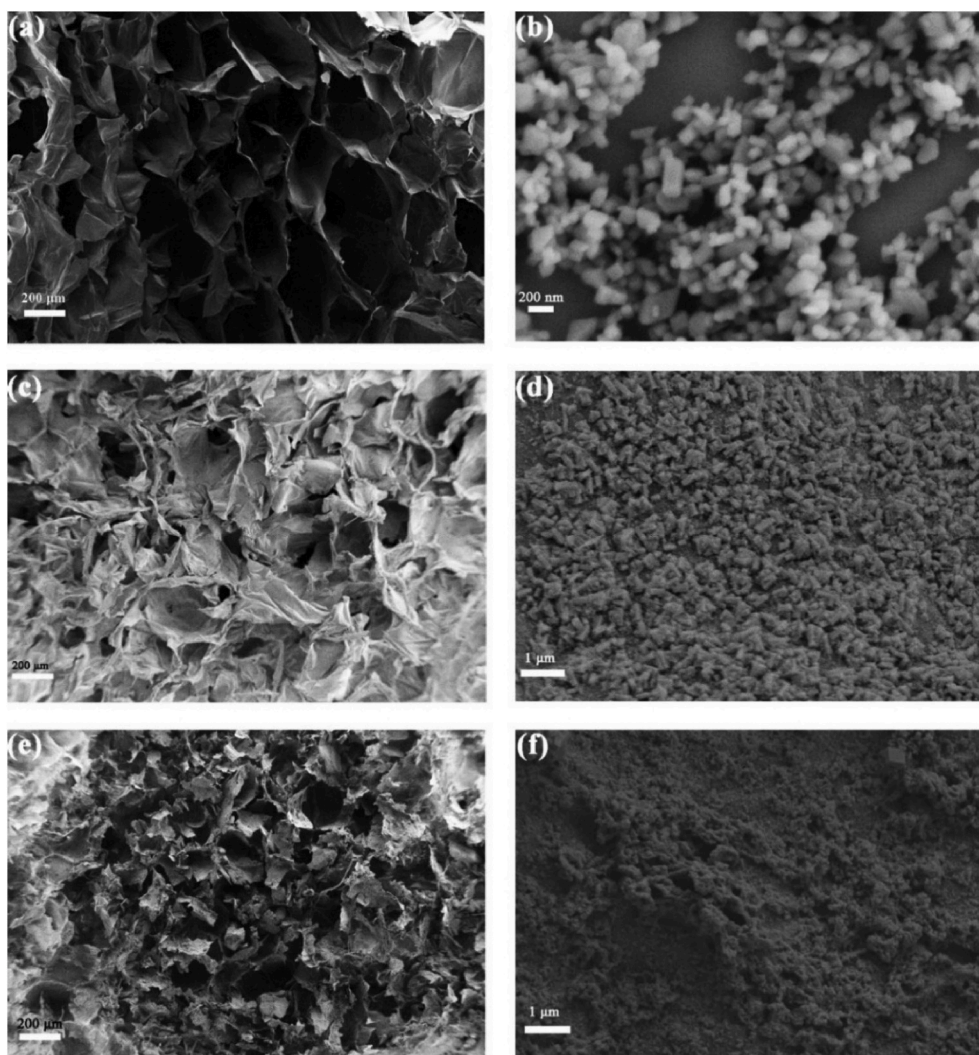


Fig. 3. (a) SEM images of CA, (b) SEM image of  $(\text{Co-Fe})^{\text{II}}(\text{pz})[\text{Ni}^{\text{II}}(\text{CN})_4]$ , (c-d) SEM images of  $\text{CoFe@CA-IS}$ , (e-f) SEM images of  $\text{CoFe@CA-D}$ .

used as an example to describe the synthetic steps of composite aerogel.

#### 2.4.1. Preparation of hybrid aerogel composite by in-situ method

First, the cellulose aerogel was immersed in a water and methanol (vol/vol = 1/1) mixture solution of 40 mL of  $\text{Co}^{2+}$ ,  $\text{Fe}^{2+}$  and pyrazine (1.5 mmol  $\text{Co}(\text{NO}_3)_2 \cdot 6\text{H}_2\text{O}$ , 1.5 mmol  $\text{Fe}(\text{ClO}_4)_2 \cdot x\text{H}_2\text{O}$  and 3 mmol pyrazine) for 4 h. The aerogel was then immersed in 10 mL of  $\text{K}_2[\text{Ni}$

$(\text{CN})_4] \cdot x\text{H}_2\text{O}$  solution for 4 h. Finally, the hybrid aerogel was washed alternately with water and methanol several times, and dried at room temperature to obtain hybrid aerogel composite, which was recorded as  $\text{CoFe@CA-IS}$ .

#### 2.4.2. Preparation of hybrid aerogel composite by doping method

The neutral gel was chopped and the mashed gel was made into a

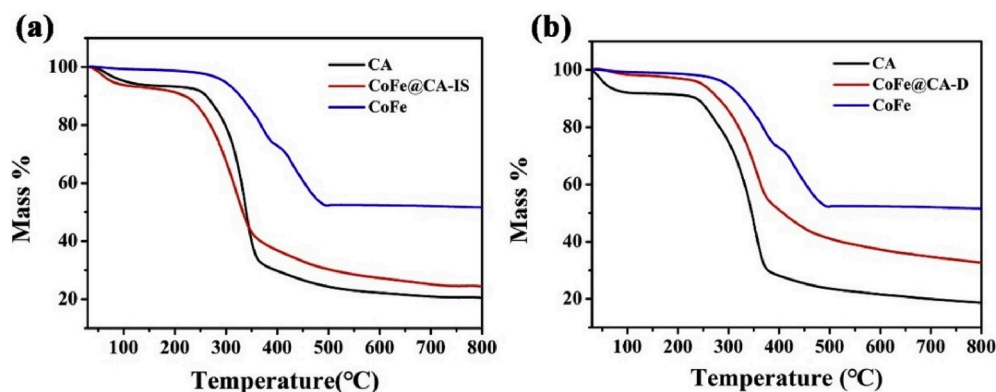


Fig. 4. (a) The TG curves of  $\text{CoFe@CA-IS}$ ; (b) the TG curves of  $\text{CoFe@CA-D}$ .

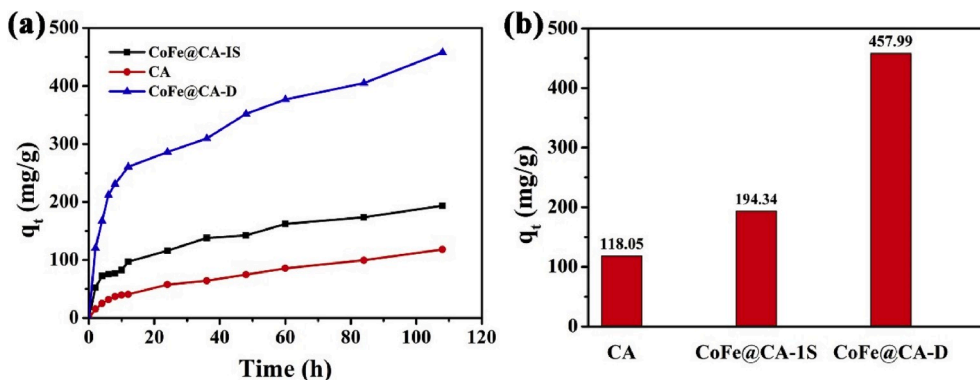


Fig. 5. (a) The adsorption curves of CA, CoFe@CA-IS and CoFe@CA-D; (b) the maximum adsorption capacity of CA, CoFe@CA-IS and CoFe@CA-D.

uniform gel fluid using a HJ-5 type multi-purpose stirrer and an over-speed shear. 1 g of  $(\text{Co-Fe})^{\text{II}}(\text{pz})[\text{Ni}^{\text{II}}(\text{CN})_4]$  was added to 50 g of the gel fluid, stirred uniformly, and then dropped into the orifice plate. After freezing at  $-20\text{ }^{\circ}\text{C}$  for 2 h, a hybrid aerogel was obtained by freeze-drying, and it was recorded as CoFe@CA-D.

## 2.5. Characterization

The surface morphologies of MOF, cellulose aerogel and hybrid aerogel were characterized by field emission scanning electron microscopy (FE-SEM, Hitachi S-4800, Japan). The crystal structures of MOF, cellulose aerogel and hybrid aerogel were analyzed by X-ray diffraction (XRD, Bruker D8, Germany) with  $\text{Cu K}\alpha$  ( $1.54056\text{ \AA}$ ) radiation (40 kV, 40 mA) in the  $2\theta$  range of  $5\text{--}40^{\circ}$  at a scanning rate of  $5^{\circ}\text{ min}^{-1}$ . The loadings of the cellulose aerogels and the thermal stability of MOF, cellulose aerogel and hybrid aerogel were characterized by thermogravimetric analyzer (TGA, Pyris Diamond I, PerkinElmer Corporation) under a nitrogen atmosphere at a heating rate of  $10\text{ }^{\circ}\text{C min}^{-1}$  and a temperature of  $30\text{--}700\text{ }^{\circ}\text{C}$ . The specific surface area of MOF was analyzed by the Brunauer-Emmett-Teller (BET). The  $\text{N}_2$  adsorption-desorption isotherm at 77 K was measured on a Micrometrics ASAP 2010 system to analyze their pore structure. All the samples were immersed methanol for 24 h and dried under vacuum at  $100\text{ }^{\circ}\text{C}$ . The MercuryIntrusion (MIR, Auto Pore IV 9500, USA) was used to calculate porosity of pure aerogels and hybrid aerogel. The chemical structures of MOF, cellulose aerogel and hybrid aerogel were analyzed by FT-IR spectrometer (Nicolet 5700, Thermo Electron Corp., USA). In the range of  $4000\text{--}400\text{ cm}^{-1}$ , it was detected by the method of KBr disk at a resolution of  $4\text{ cm}^{-1}$ .

## 2.6. Adsorption experiment

The adsorption experiment was carried out as following: 10 mg activated MOF or 50 mg activated CA or hybrid aerogel was dispersed in 50 mL of a solution of iodine/hexane ( $3 \times 10^{-3}\text{ M}$ ), the adsorption test was starting at various time. The concentration at different times was tested by UV-Vis spectrophotometer (UV, Hitachi U-3900, Japan) at 522 nm. The adsorption capacity at time  $t$  was calculated using the following equation:

$$q_t = \frac{(C_0 - C_t)V}{m} \quad (1)$$

where  $C_0$  was the initial concentration,  $C_t$  was the concentration at time  $t$ ,  $V$  was the iodine solution volume,  $m$  was the mass of CA, MOF, or hybrid aerogel.

The adsorption mechanism was studied by adsorption kinetics. The adsorption rate constant is obtained from the pseudo-first-order equation, which is showed below:

$$\ln(q_e - q_t) = \ln q_e - k_1 t \quad (2)$$

Where  $q_e$  was the adsorption capacities ( $\text{mg g}^{-1}$ ) at time equilibrium,  $q_t$  was the adsorption capacities ( $\text{mg g}^{-1}$ ) at time  $t$ .  $k_1$  was the pseudo-first-order rate constant. From the plots of  $\ln(q_e - q_t)$  versus  $t$ , the values of  $k_1$  and  $q_e$  were determined.

The pseudo-second-order equation represented by linearization was as follows:

$$\frac{t}{q_t} = \frac{1}{k_2 q_e^2} + \frac{t}{q_e} \quad (3)$$

Where  $q_e$  was the adsorption capacities ( $\text{mg g}^{-1}$ ) at time equilibrium,  $q_t$  was the adsorption capacities ( $\text{mg g}^{-1}$ ) at time  $t$ .  $k_2$  was the pseudo-second-order rate constant, and was determined from the linear plot of  $t/q_t$  versus  $t$ .

## 3. Results and discussions

The structures and iodine adsorption properties of the three bimetal Hofmann-type MOF are showed in Fig. S1. It could be known from Fig. S1(b) that  $(\text{Co-Fe})^{\text{II}}(\text{pz})[\text{Ni}^{\text{II}}(\text{CN})_4]$  had the best adsorption performance for iodine, and the adsorption capacity reached up to  $1149.27\text{ mg g}^{-1}$ . Therefore, this article mainly discussed the structure and performance of CoFe@CA.

### 3.1. Characterization of hybrid aerogel

Photographs of CA, CoFe@CA and  $(\text{Co-Fe})^{\text{II}}(\text{pz})[\text{Ni}^{\text{II}}(\text{CN})_4]$  are showed in Fig. 1. It can be clearly seen that the hybrid aerogel has become as bright orange as  $(\text{Co-Fe})^{\text{II}}(\text{pz})[\text{Ni}^{\text{II}}(\text{CN})_4]$  compare with the pure aerogel. The XRD pattern of the hybrid aerogels is showed in Fig. 2. It is found that the diffraction peaks of hybrid aerogels contained both the diffraction peaks of MOFs and cellulose aerogel, which proved that the MOF had been successfully loaded onto the aerogel. Compared to pure MOF, some diffraction peaks of the hybrid aerogel become weak or even disappear, suggesting that MOF particles were encapsulated in cellulose. It can be seen from Fig. 3 (a) that the pure aerogel is porous structure with smooth pore walls. At the same time, the morphology of  $(\text{Co-Fe})^{\text{II}}(\text{pz})[\text{Ni}^{\text{II}}(\text{CN})_4]$  is nanoparticle with a size of about 100 nm as shown in Fig. 3 (b). The CoFe@CA-IS maintains the porosity while the  $(\text{Co-Fe})^{\text{II}}(\text{pz})[\text{Ni}^{\text{II}}(\text{CN})_4]$  particles are well grown on the aerogel wall (Fig. 3 (c) and (d)). Compared to  $(\text{Co-Fe})^{\text{II}}(\text{pz})[\text{Ni}^{\text{II}}(\text{CN})_4]$ , the grain size on the aerogel wall is large, suggesting that aerogel affects the growth of  $(\text{Co-Fe})^{\text{II}}(\text{pz})[\text{Ni}^{\text{II}}(\text{CN})_4]$  crystals. Similarly, the CoFe@CA-D maintains the porosity of the aerogel while successfully loading the  $(\text{Co-Fe})^{\text{II}}(\text{pz})[\text{Ni}^{\text{II}}(\text{CN})_4]$  (Fig. 3 (e) and (f)). The loading of the hybrid aerogels prepared by different methods was analyzed by thermogravimetry. The results demonstrate that the loading of CoFe@CA-IS is 13.56%, while

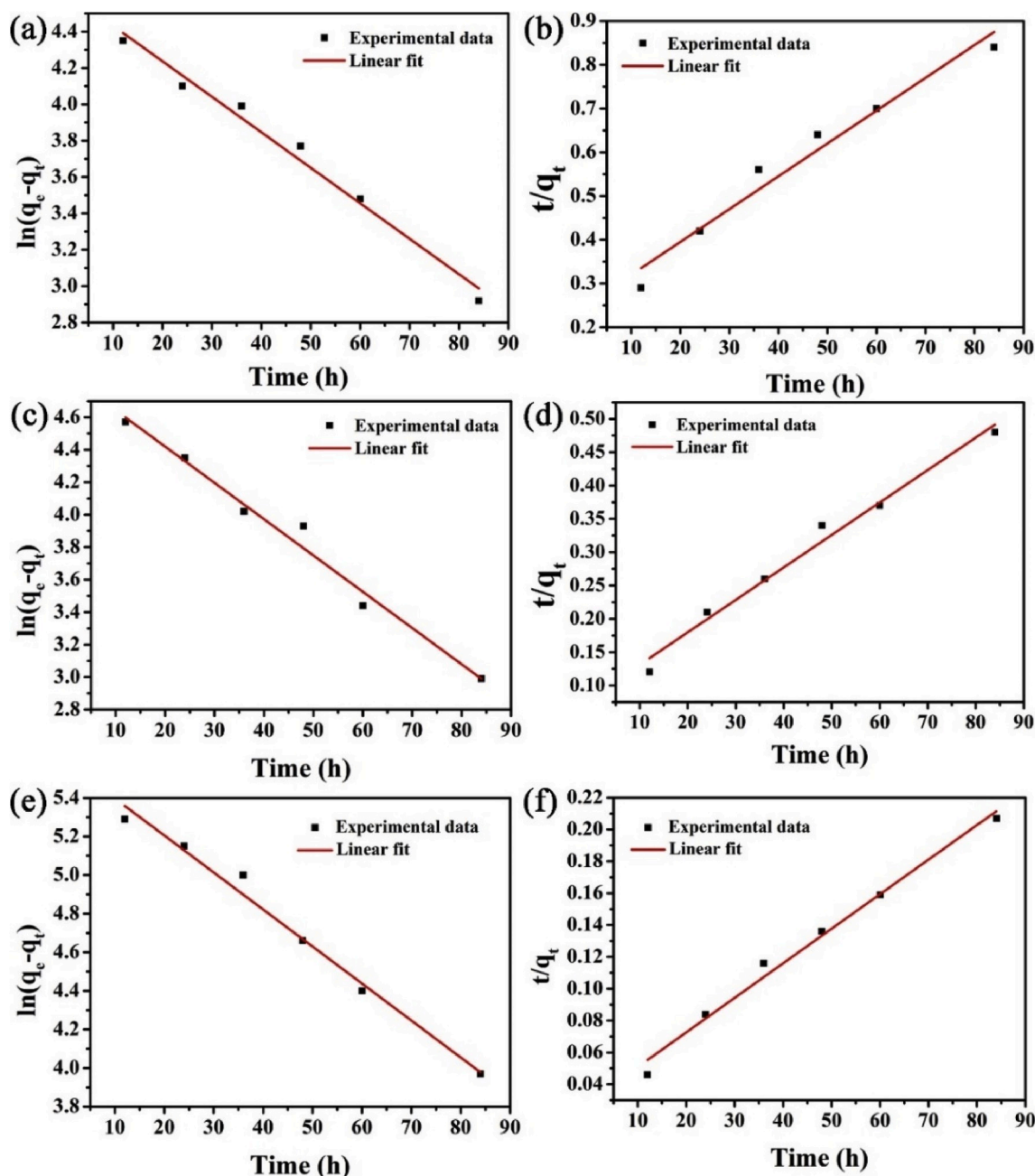


Fig. 6. (a–b) Pseudo-first-order and pseudo-second-order kinetics of CA, respectively. (c–d) pseudo-first-order and pseudo-second-order-kinetics of CoFe@CA-IS, respectively. (e–f) pseudo-first-order and pseudo-second-order kinetics of CoFe@CA-D respectively.

**Table 1**  
Kinetics of adsorption of iodine by CA, CoFe@CA-IS and CoFe@CA-D

| Sorbents   | Pseudo-first-order kinetics |                             |       | Pseudo-second-order kinetics                |                             |       | $q_{(\text{exp})}$ (mg g <sup>-1</sup> ) |
|------------|-----------------------------|-----------------------------|-------|---|-----------------------------|-------|--|
|            | $K_1$ (h <sup>-1</sup> )    | $q_e$ (mg g <sup>-1</sup> ) | $R^2$ | $K_2$ (g mg <sup>-1</sup> h <sup>-1</sup> ) | $q_e$ (mg g <sup>-1</sup> ) | $R^2$ |  |
| CoFe@CA-IS | 0.0223                      | 129.80                      | 0.979 | $2.88 \times 10^{-4}$                       | 205.34                      | 0.980 | 194.34                                   |
| CoFe@CA-D  | 0.0208                      | 292.38                      | 0.971 | $3.06 \times 10^{-4}$                       | 423.73                      | 0.988 | 457.99                                   |
| CA         | 0.0195                      | 102.19                      | 0.980 | $2.3 \times 10^{-4}$                        | 133.33                      | 0.958 | 118.05                                   |

the loading of CoFe@CA-D is 45.80% (Fig. 4 and Table S1). The doping method significantly increases the loading of MOF in the hybrid aerogels. The addition of (Co–Fe)<sup>II</sup>(pz)[Ni<sup>II</sup>(CN)<sub>4</sub>] greatly increases the porosity of the hybrid aerogel (Table S2). The porosity of CoFe@CA-IS and CoFe@CA-D increases from 45.7% to 86.7% and 87.8%, respectively, and the pore volume of CoFe@CA-IS and CoFe@CA-D increases

from 0.407 mL g<sup>-1</sup> to 6.040 and 8.081 mL g<sup>-1</sup>, respectively. The BET surface area of the (Co–Fe)<sup>II</sup>(pz)[Ni<sup>II</sup>(CN)<sub>4</sub>] is 395.9 m<sup>2</sup> g<sup>-1</sup> (Fig. S2). The pore volume is 0.318 mL g<sup>-1</sup>, and the pore size is 3.212 nm.

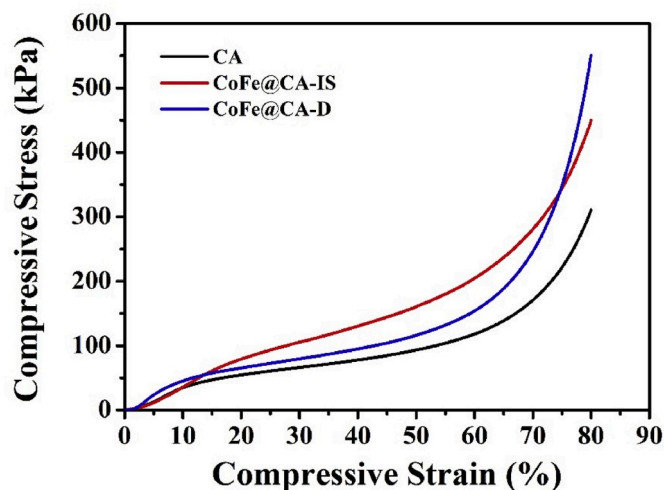


Fig. 7. Compressive stress-strain curves of CA, CoFe@CA-IS and CoFe@CA-D.

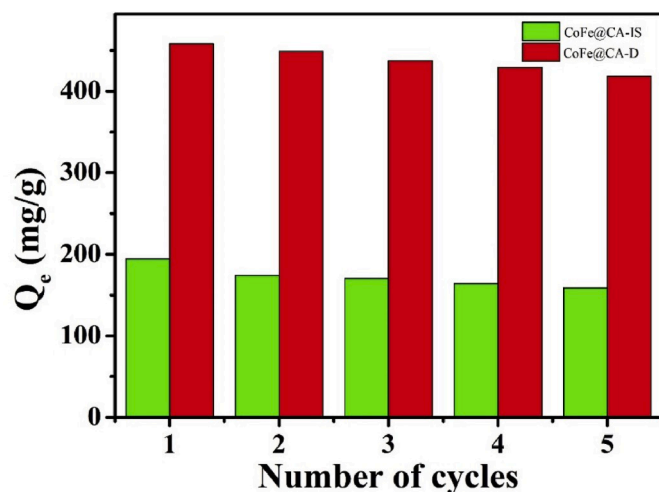


Fig. 8. Adsorption capacity of iodine by CoFe@CA-IS and CoFe@CA-D after different cycles.

### 3.2. Adsorption performance analysis

The adsorption capacity of CoFe@CA was tested at different time periods to study the adsorption kinetics (see adsorption experiment for details). The adsorption curves of CA, CoFe@CA and the maximum adsorption amount are obtained (Fig. 5). The maximum adsorption capacities of CoFe@CA-IS and CoFe@CA-D are 194.34 and 457.99  $\text{mg g}^{-1}$ , respectively, which was significantly higher than 118.05  $\text{mg g}^{-1}$  of CA, as shown in Fig. 5 (b).

The adsorption kinetics and the kinetic parameters of CA, CoFe@CA-IS, CoFe@CA-D are showed in Fig. 6 and Table 1, respectively. Among them, the adsorption process of iodine by pure aerogel is more consistent with pseudo-first-order kinetics. The pseudo-first-order kinetics of a pure aerogel has a  $R^2$  of 0.980, which is greater than the pseudo-second-order kinetics of  $R^2$  (0.958). The adsorption process is more in line with the pseudo-first-order dynamics. The equilibrium adsorption amount are measured by the experiment (118.05  $\text{mg g}^{-1}$ ), which is also close to the equilibrium adsorption amount of the pseudo-first-order calculation (102.19  $\text{mg g}^{-1}$ ). Different from the adsorption behavior of pure aerogel, the adsorption behavior of hybrid aerogel is consistent with pseudo-second-order kinetics. The pseudo-second-order kinetics  $R^2$  values of CoFe@CA-IS and CoFe@CA-D adsorbed iodine reached 0.980 and 0.988. The pseudo-first-order kinetic  $R^2$  values of CoFe@CA-IS and

CoFe@CA-D adsorbed iodine reach 0.979 and 0.971, respectively. These results indicate that the time dependence of adsorption fits well to the pseudo-second-order kinetic model with a rate constant of  $K_2$ . The equilibrium adsorption amounts of CoFe@CA-IS and CoFe@CA-D are 194.34 and 457.99  $\text{mg g}^{-1}$ , respectively, which are closer to the equilibrium adsorption amount calculated by pseudo-second-order kinetics (205.34 and 423.73  $\text{mg g}^{-1}$ ).

The difference in the amount of adsorption is mainly caused by the difference in the amount of MOF loaded. The doping method can further increase the loading of MOF compared to the in-situ growth method. The loading amount of MOF plays a key role in the adsorption of the hybrid aerogels.

### 3.3. Reusability of CoFe@CA-IS and CoFe@CA-D

The reusability of hybrid aerogels is a research focus of this work. Under the same conditions, the hybrid aerogel was immersed in the iodine solution, after reaching the adsorption equilibrium, the aerogel was removed and then the adsorption amount was calculated. The hybrid aerogel was then immersed into ethanol solution, heated at 80 °C for one day, the adsorbed iodine was eluted, and dried for the next cycle. The mechanical properties of CA, CoFe@CA-IS and CoFe@CA-D are illustrated in Fig. 7. The aerogel loaded with  $(\text{Co-Fe})^{\text{II}}(\text{pz})[\text{Ni}^{\text{II}}(\text{CN})_4]$  present good compression properties. When compressed to 80% deformation, the stresses of CoFe@CA-IS and CoFe@CA-D are 450 and 550 kPa, respectively, which is a significant improvement compared to the CA (310 kPa). The morphology and adsorption properties of the hybrid aerogel were analyzed after 5 cycles. The morphology of the hybrid aerogel after 5 cycles is showed in Fig. S3. After 5 cycles, the hybrid aerogel remained a porous structure, and the  $(\text{Co-Fe})^{\text{II}}(\text{pz})[\text{Ni}^{\text{II}}(\text{CN})_4]$  particles on the pore walls was still exist. The  $(\text{Co-Fe})^{\text{II}}(\text{pz})[\text{Ni}^{\text{II}}(\text{CN})_4]$  particles on the CoFe@CA-IS pore wall were slightly reduced, which may had fallen off during the elution of iodine. However, the pore walls of CoFe@CA-D were still filled with nano-sized  $(\text{Co-Fe})^{\text{II}}(\text{pz})[\text{Ni}^{\text{II}}(\text{CN})_4]$  particles. These results indicate that the doping method can well immobilize  $(\text{Co-Fe})^{\text{II}}(\text{pz})[\text{Ni}^{\text{II}}(\text{CN})_4]$  particles on the cellulose aerogel. The characteristic diffraction peaks of  $(\text{Co-Fe})^{\text{II}}(\text{pz})[\text{Ni}^{\text{II}}(\text{CN})_4]$  were still exist in the hybrid aerogel after 5 cycles. The weakening or even disappearance of the  $(\text{Co-Fe})^{\text{II}}(\text{pz})[\text{Ni}^{\text{II}}(\text{CN})_4]$  diffraction peak can be attributed to the shedding of  $(\text{Co-Fe})^{\text{II}}(\text{pz})[\text{Ni}^{\text{II}}(\text{CN})_4]$  particles. As shown in Fig. 8, as the number of cycles increases, the adsorption capacities of CoFe@CA-IS and CoFe@CA-D at the fifth cycle were still 158.65 and 418.54  $\text{mg g}^{-1}$ , respectively, maintaining 81% and 91% of the first adsorption. The result shows that CoFe@CA-IS and CoFe@CA-D have good recycling performance.

### 3.4. Adsorption mechanism of hybrid aerogel

It can be known from the adsorption kinetics that the physical adsorption is mainly in accordance with the pseudo-first-order kinetic process, and the chemisorption is mainly base on the pseudo-second-order kinetic process [39]. As shown in Fig. 5, the addition of  $(\text{Co-Fe})^{\text{II}}(\text{pz})[\text{Ni}^{\text{II}}(\text{CN})_4]$  converts the adsorption of iodine on the aerogel from physical adsorption to chemisorption, so  $(\text{Co-Fe})^{\text{II}}(\text{pz})[\text{Ni}^{\text{II}}(\text{CN})_4]$  is a major contributor. The XRD and FT-IR of  $(\text{Co-Fe})^{\text{II}}(\text{pz})[\text{Ni}^{\text{II}}(\text{CN})_4]$  before and after adsorption were carried out. As can be seen from Fig. 9 (a), the crystal structure of  $(\text{Co-Fe})^{\text{II}}(\text{pz})[\text{Ni}^{\text{II}}(\text{CN})_4]$  does not change after adsorption, indicating that iodine does not destroy the structure of  $(\text{Co-Fe})^{\text{II}}(\text{pz})[\text{Ni}^{\text{II}}(\text{CN})_4]$ . It can be seen from Fig. 9 (b) that no new infrared absorption peak appears after adsorption, which indicate that iodine has not reacted with  $(\text{Co-Fe})^{\text{II}}(\text{pz})[\text{Ni}^{\text{II}}(\text{CN})_4]$ . After iodine adsorption, the stretching vibration of  $\nu$  (CN) changed from 2144  $\text{cm}^{-1}$  to 2175  $\text{cm}^{-1}$  (Fig. 9 (c)). The addition of iodine strengthen the weak  $\sigma$  ( $\text{Co}^{\text{II}}-\text{CN}$ ) and  $\sigma$  ( $\text{Fe}^{\text{II}}-\text{CN}$ ), which cause the  $\nu$  (CN) to move to a high wave number [40]. As shown in Fig. 9 (d), the  $\nu$  ( $\text{M-N}_{\text{pyrazine}}$ ) also moves slightly before and after adsorption, which indicates that there is a weak

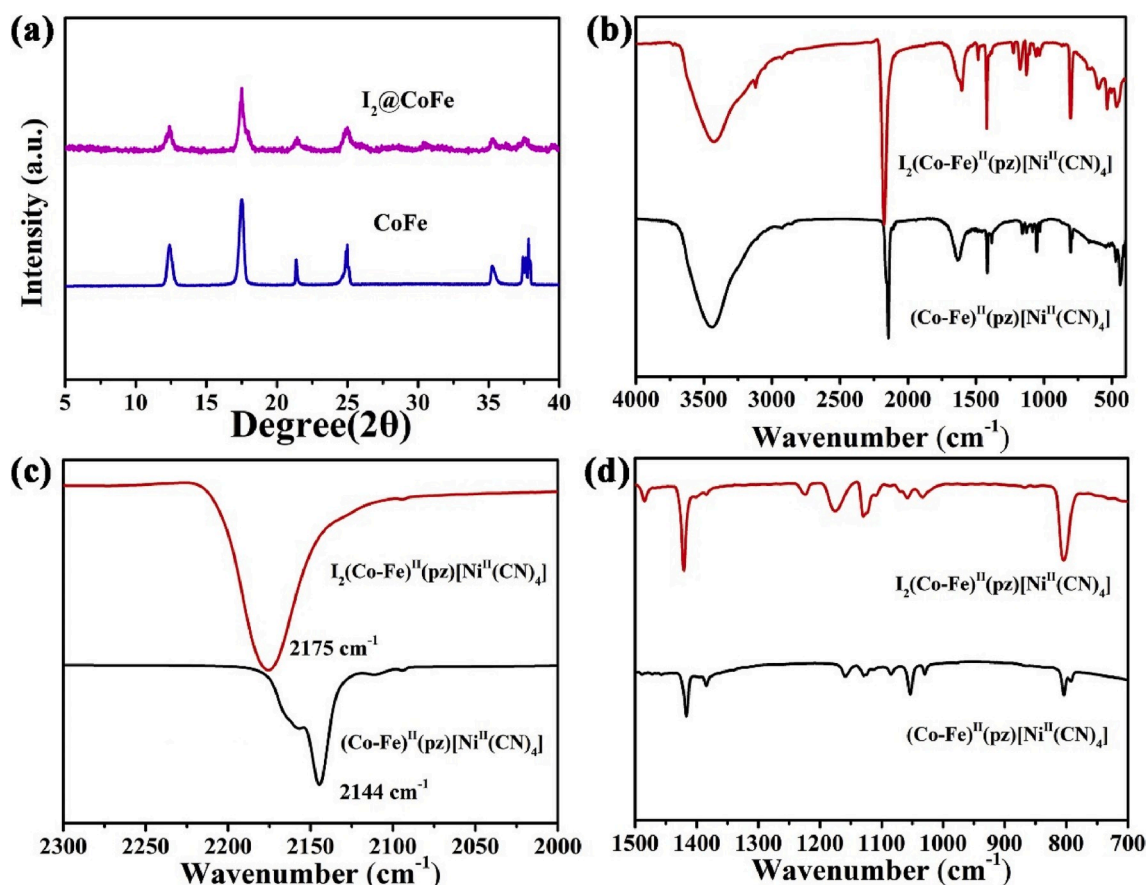


Fig. 9. (a) XRD pattern of  $(\text{Co-Fe})^{\text{II}}(\text{pz})[\text{Ni}^{\text{II}}(\text{CN})_4]$  before and after adsorption; (b) Infrared image before and after adsorption of  $(\text{Co-Fe})^{\text{II}}(\text{pz})[\text{Ni}^{\text{II}}(\text{CN})_4]$ ; (c) infrared absorption peak of cyano group before and after adsorption; (d) infrared absorption peak of pyrazine before and after adsorption.

interaction between iodine and pyrazine. Therefore, we believe that the weak electrostatic interaction between iodine with both cyano and pyrazine is the main adsorption mechanism.

#### 4. Conclusion

In this paper, two kinds of hybrid aerogels loading with  $(\text{Co-Fe})^{\text{II}}(\text{pz})[\text{Ni}^{\text{II}}(\text{CN})_4]$  were successfully prepared by in-situ growth method and doping method, respectively. Compared with the in-situ growth method, the doping method could significantly increase the loading of  $(\text{Co-Fe})^{\text{II}}(\text{pz})[\text{Ni}^{\text{II}}(\text{CN})_4]$  nanoparticles, which was increased from 13.56% to 45.80%. The hybrid aerogels were employed for adsorption of iodine. The  $\text{CoFe@CA-D}$  exhibited a higher maximum adsorption capacity ( $457.99 \text{ mg g}^{-1}$ ) than  $\text{CoFe@CA-IS}$  ( $194.34 \text{ mg g}^{-1}$ ). Furthermore, the adsorption efficiency of  $\text{CoFe@CA-D}$  was still retain 90% after 5 cycles of iodine release and uptake. The hybrid aerogels are potential alternative materials to capture iodine, and the doping method provides a new strategy for preparing efficient and environmentally friendly hybrid aerogels.

#### Declaration of competing interest

The authors declare that they have no known competing financial interests or personal relationships that could have appeared to influence the work reported in this paper.

#### Acknowledgments

This work is supported by the National Natural Science Foundation of China (51672251) and Science Foundation of Zhejiang Sci-Tech

University (ZSTU) under Grant No. 13012138-Y.

#### Appendix A. Supplementary data

Supplementary data to this article can be found online at <https://doi.org/10.1016/j.micromeso.2020.110386>.

#### References

- [1] C. Li, H. Xu, J. Gao, W. Du, L. Shangguan, X. Zhang, R.-B. Lin, H. Wu, W. Zhou, X. Liu, *J. Mater. Chem. A* 7 (2019) 11928–11933.
- [2] C. Acar, I. Dincer, *J. Clean. Prod.* 218 (2019) 835–849.
- [3] W. Luo, G. Xiao, F. Tian, J.J. Richardson, Y. Wang, J. Zhou, J. Guo, X. Liao, B. Shi, *Energy Environ. Sci.* 12 (2019) 607–614.
- [4] Y. Xie, C. Chen, X. Ren, X. Wang, H. Wang, X. Wang, *Prog. Mater. Sci.* 103 (2019) 180–234.
- [5] B. Li, B. Wang, X. Huang, L. Dai, L. Cui, J. Li, X. Jia, C. Li, *Angew. Chem. Int. Ed.* 58 (2019) 3885–3889.
- [6] H. Sun, B. Yang, A. Li, *Chem. Eng. J.* 372 (2019) 65–73.
- [7] P. Wang, Q. Xu, Z. Li, W. Jiang, Q. Jiang, D. Jiang, *Adv. Mater.* 30 (2018) 1801991.
- [8] M. Xu, T. Wang, L. Zhou, D. Hua, *J. Mater. Chem. A* 8 (2020) 1966–1974.
- [9] P. Chen, X. He, M. Pang, X. Dong, S. Zhao, W. Zhang, *ACS Appl. Mater. Interfaces* 12 (2020) 20429–20439.
- [10] H. Li, Y. Li, B. Li, D. Liu, Y. Zhou, *Chemosphere* 252 (2020), 126448.
- [11] Z.-J. Li, Z. Yue, Y. Ju, X. Wu, Y. Ren, S. Wang, Y. Li, Z.-H. Zhang, X. Guo, J. Lin, J.-Q. Wang, *Inorg. Chem.* 59 (2020) 4435–4442.
- [12] B. Karadeniz, D. Žilić, I. Huskić, L.S. Germann, A.M. Fidelli, S. Muratović, I. Lončarić, M. Etter, R.E. Dinnebier, D. Barišić, *J. Appl. Comput. Sci.* 141 (2019) 19214–19220.
- [13] D. Sun, P.R. Adiyala, S.J. Yim, D.P. Kim, *Angew. Chem.* 131 (2019) 7483–7487.
- [14] G. Skorupskii, B.A. Trump, T.W. Kasel, C.M. Brown, C.H. Hendon, M. Dincă, *Nat. Chem.* 12 (2020) 131–136.
- [15] L. Chen, D. Liu, J. Peng, Q. Du, H. He, *Coord. Chem. Rev.* 404 (2020) 213113.
- [16] Y. Li, T. Zhao, M. Lu, Y. Wu, Y. Xie, H. Xu, J. Gao, J. Yao, G. Qian, Q. Zhang, *Small* 15 (2019) 1901940.
- [17] L. Zhang, S. Jee, J. Park, M. Jung, D. Wallacher, A. Franz, W. Lee, M. Yoon, K. Choi, M. Hirscher, *J. Am. Chem. Soc.* 141 (2019) 19850–19858.

- [18] H. Xiang, A. Ameen, P. Gorgojo, F.R. Siperstein, S.M. Holmes, X. Fan, *Microporous Mesoporous Mater.* 292 (2020) 109724.
- [19] J. Wang, S. Zhuang, *Coord. Chem. Rev.* (2019) 400.
- [20] Y. Wang, J. Tao, S. Xiong, P. Lu, J. Tang, J. He, M.U. Javaid, C. Pan, G. Yu, *Chem. Eng. J.* 380 (2020).
- [21] Q. Zhao, L. Zhu, G. Lin, G. Chen, B. Liu, L. Zhang, T. Duan, J. Lei, *ACS Appl. Mater. Interfaces* 11 (2019) 42635–42645.
- [22] B. Zheng, X. Lin, X. Zhang, D. Wu, K. Matyjaszewski, *Adv. Funct. Mater.* (2019) 1907006.
- [23] Y. Yu, L. Ren, M. Liu, S. Huang, X. Xiao, R. Liu, L. Wang, W. Xu, *ACS Appl. Mater. Interfaces* 11 (2019) 31291–31301.
- [24] S. Sakaida, T. Haraguchi, K. Otsubo, O. Sakata, A. Fujiwara, H. Kitagawa, *Inorg. Chem.* 56 (2017) 7606–7609.
- [25] G. Massasso, J.r.m. Long, C. Guerin, A.s. Grandjean, B. Onida, Y. Guari, J. Larionova, G. Maurin, S. Devautour-Vinot, *J. Phys. Chem. C* 119 (2015) 9395–9401.
- [26] Q. Huo, J. Li, G. Liu, X. Qi, X. Zhang, Y. Ning, B. Zhang, Y. Fu, S. Liu, *Chem. Eng. J.* 362 (2019) 287–297.
- [27] Y. Gu, D. Xie, Y. Wang, W. Qin, H. Zhang, G. Wang, Y. Zhang, H. Zhao, *Chem. Eng. J.* 357 (2019) 579–588.
- [28] H. Zhu, X. Yang, E.D. Cranston, S. Zhu, *Adv. Mater.* 28 (2016) 7652–7657.
- [29] L. Wang, H. Xu, J. Gao, J. Yao, Q. Zhang, *Coord. Chem. Rev.* 398 (2019) 213016.
- [30] G. Huang, D. Xu, Z. Qin, Q. Liang, C. Xu, B. Lin, *Chem. Eng. J.* 395 (2020) 125181.
- [31] S.A. Ogundare, W.E. van Zyl, *Cellulose* 26 (2019) 6489–6528.
- [32] Y. Li, L. Zhu, N. Grishkewich, K.C. Tam, J. Yuan, Z. Mao, X. Sui, *ACS Appl. Mater. Interfaces* 11 (2019) 9367–9373.
- [33] A. Bernardes, V. Pellegrini, F. Curtolo, C. Camilo, B. Mello, M. Johns, J. Scott, F. Guimaraes, I. Polikarpov, *Carbohydr. Polym.* 211 (2019) 57–68.
- [34] Y. Yang, Q. Huang, G.F. Payne, R. Sun, X. Wang, *Nanoscale* 11 (2019) 725–732.
- [35] C. Cai, Z. Wei, Y. Huang, C. Ding, P. Wang, J. Song, L. Deng, Y. Fu, W. Zhong, *ACS Appl. Mater. Interfaces* 12 (2020) 11273–11286.
- [36] Z. Zeng, T. Wu, D. Han, Q. Ren, G. Siqueira, G. Nyström, *ACS Nano* 14 (2020) 2927–2938.
- [37] C. Lei, J. Gao, W. Ren, Y. Xie, S.Y.H. Abdalkarim, S. Wang, Q. Ni, J. Yao, *Carbohydr. Polym.* 205 (2019) 35–41.
- [38] W. Ren, J. Gao, C. Lei, Y. Xie, Y. Cai, Q. Ni, J. Yao, *Chem. Eng. J.* 349 (2018) 766–774.
- [39] X. Chen, L. Liu, Z. Luo, J. Shen, Q. Ni, J. Yao, *React. Funct. Polym.* 125 (2018) 77–83.
- [40] G. Massasso, M. Rodríguez-Castillo, J. Long, J. Haines, S. Devautour-Vinot, G. Maurin, A. Grandjean, B. Onida, B. Donnadieu, J. Larionova, *Dalton Trans.* 44 (2015) 19357–19369.